Research Square

Preprints are preliminary reports that have not undergone peer review.
They should not be considered conclusive, used to inform clinical practice,
or referenced by the media as validated information.

Real-time neutron monitoring for boron neutron capture therapy using 10B-integrated hybrid perovskite thin-film sensors

Yasuki Okuno

yasuki.okuno.c6@tohoku.ac.jp

Tohoku University https://orcid.org/0000-0002-8569-4077

Yoshinori Nakayama

RIKEN

Tomohiro Kobayashi

RIKEN

Yoshie Otake

RIKEN

Hiroki Sugimoto

PXP Corporation

Motoshi Nakamura

PXP Corporation

Masahiro Hino

Kyoto University

Tatsuro Oda

The University of Tokyo

Yoshinori Katanaya

Toyohashi University of Technology

Keisuke Yamane

Toyohashi University of Technology

Article

Keywords:

Posted Date: March 5th, 2026

DOI: https://doi.org/10.21203/rs.3.rs-8897906/v1

License: This work is licensed under a Creative Commons Attribution 4.0 International License.
Read Full License

Additional Declarations: There is **NO** Competing Interest.

Real-time neutron monitoring for boron neutron capture therapy using ^{10}B-integrated hybrid perovskite thin-film sensors

Yasuki Okuno[1,2,*], Yoshinori Nakayama[1], Tomohiro Kobayashi[1], Yoshie Otake[1], Hiroki Sugimoto[3], Motoshi Nakamura[3], Masahiro Hino[4], Tatsuro Oda[5], Yoshinori Katanaya[6] & Keisuke Yamane[6]

Affiliations

[1]RIKEN Center for Advanced Photonics, Saitama, Japan

[2]Tohoku University, Miyagi, Japan

[3]PXP Corporation, Kanagawa, Japan

[4]Kyoto University, KURNS, Osaka, Japan

[5]Tokyo University, Tokyo, Japan

[6]Toyohashi University of Technology, Aichi, Japan

[*]Corresponding author

Correspondence to: Yasuki Okuno

E-mail : yasuki.okuno@riken.jp

Contributions

Y.O. performed neutron irradiation experiments, analyzed the data, and wrote the manuscript. Y.N. prepared the ^{10}B conversion films. T.T. carried out the simulations. Y.Ot. supervised the project. H.S. fabricated the HOIP/perovskite devices. M.H. conducted cold-neutron irradiation

tests at the MINE beamline. T.O. analyzed neutron transmission data. Y.K. contributed to data analysis and interpretation. K.Y. contributed to the discussion and manuscript revision.

Abstract

Hybrid organic–inorganic perovskites (HOIPs) are leading candidates for next-generation optoelectronics, driving rapid advancements in efficiency and applications, such as neutron detectors, due to their exceptional optoelectronic properties, including high-charge mobility and high-flux capability. High-flux neutron detector architectures have been investigated for real-time dosimetry; however, robust devices suitable for boron neutron capture therapy (BNCT) remain limited. In this study, we present the use of HOIP thin-film sensors integrated with developed ^{10}B conversion layer for neutron detection in BNCT monitoring. A self-biased ITO/SnO2/$FAPbI_3$/Spiro-OMeTAD device was laser-patterned to a 5 × 5 mm^2 active area and coupled with an electrosprayed ^{10}B film having an equivalent thickness of 3.3 μm, which was optimized based on cold-neutron transmission measurements. Air gap elimination between the converter and Au electrode markedly increased neutron sensitivity. In the KUR-HWNIF BNCT field, converted devices yielded nA-level currents that were linear with neutron flux up to ~10^9 s^{-1} cm^{-2}. The γ-noise fraction of ~0.012% facilitated 1-s real-time readout and stable signal performance at neutron fluences up to 10^{13} cm^{-2}. The stability, combined with negligible post-irradiation current–voltage changes, establishes converted HOIP thin-film sensors as flexible, self-diagnosable real-time BNCT neutron monitors suitable for clinical use.

Introduction

Neutron detectors are gaining considerable attention due to their use across a wide range of fields, such as nuclear security[1-5], nondestructive inspection of critical structures[6-9], and boron neutron capture therapy (BNCT)[10-13]. A detector must fulfil requirements defined by the specific application. The main characteristics of a detector involve the covered energy range, sensitivity, noise, and linear response. In addition, the flexibility and portability of a detector for monitoring tasks add value, as it broadens the potential use cases. As neutrons are uncharged, their direct detection is intrinsically difficult; hence, practical neutron metrology generally relies on nuclides with large reaction cross sections—such as ^{3}He, ^{6}Li, ^{10}B, and ^{197}Au—to convert incident neutrons into secondary charged particles or γ-rays that can be measured. Although diverse detection principles have been established, including scintillators, gas counters, semiconductor detectors, and activation methods, the choice of effective converter nuclides remains limited[14-20]. Moreover, in high-flux neutron environments, detector-signal saturation, radiation-induced degradation, and the need to discriminate γ-ray backgrounds become pronounced, making it challenging for existing approaches to simultaneously satisfy specific requirements.

In the context of BNCT, the limitations are particularly critical, as therapeutic efficacy and safety depend on real-time, high-accuracy characterization of the neutron field[21], wherein clinical guidelines[22] specify stringent performance targets, such as neutron fluxes of ~10^{9} s^{-1} cm^{-2}, fluences on the order of 10^{13} cm^{-2}, spatial resolution greater than 5 mm^{2}, and measurement errors less than 5%. Currently, dose evaluation commonly employs ^{197}Au activation[23-26] and $LiCaAlF_6$(LiCAF)-based detectors[21,27,28]; however, the former lacks real-time capability whereas the latter cannot self-diagnose detector integrity during irradiation, complicating reliability assessment under prolonged high-flux exposure. Consequently, there is a strong need for new neutron sensors that can provide robust, real-time measurements under BNCT-relevant conditions.

Recently, hybrid organic–inorganic perovskites (HOIPs) have attracted considerable attention as platform materials for space and radiation-related devices[29-33] due to their facile low-temperature thin-film processing[34-37] and laser-enabled patterning versatility[38-41]. We had previously predicted that integrating a boron neutron-conversion layer into HOIP thin-film devices[42,43] enables real-time neutron sensing even in high-flux fields of 10^6–10^{13} s^{-1} cm^{-2}. Moreover, HOIP-based sensors offer practical advantages well aligned with BNCT demands, such as flexible substrates that allow wearable and conformal implementations, pre-/post-use current–voltage (I–V) characterization that enables straightforward integrity checks, and laser patterning that permits geometry optimization tailored to specific anatomical sites, which are capabilities difficult to realize with conventional detectors. In this study, we develop the device architecture (active area, electrode configuration, and encapsulation) and ^{10}B conversion-layer parameters (thickness and deposition conditions) of conversion-layer-integrated HOIP sensors. We systematically evaluate the neutron response and γ-ray noise characteristics within BNCT fields. By benchmarking performance against clinical guidelines, we clarify the detection behavior and operational limits required for accurate, real-time performance under high-flux irradiation, thereby establishing HOIP thin-film sensors as a compelling option for real-time neutron metrology in BNCT environments.

Results and Discussion

Optimization of HOIP sensor architecture for neutron detection

The steps to prepare the HOIP-based neutron sensor include HOIP photovoltaic device fabrication, ^{10}B neutron-conversion film deposition on a polyimide substrate, and assembly of both components to create the complete sensor, followed by characterization of the assembly responses

under neutron and γ-ray irradiation. The HOIP device was fabricated with an FTO glass/SnO_2/$Cs_{0.05}FA_{0.95}PbI_3$/HTL/ITO multilayer structure (Fig. 1a), mimicking a solar-cell configuration that enables self-biased operation. Using laser patterning (Fig. 1b), the active area was defined as 5 × 5 mm^2, consistent with the BNCT clinical guidelines requiring position sensitivity within this scale. Gold electrodes were subsequently fabricated on the HOIP device by a thermal evaporator (Fig. 1c).

The ^{10}B neutron-conversion film was deposited onto a polyimide substrate via electrospray coating (Fig. 1d) and trimmed to 6 × 6 mm^2 to cover the entire HOIP active area (Fig. 1e). Previous studies on thin-film neutron converters indicate that an effective ^{10}B thickness of 3–4 μm (at theoretical density) maximizes detection efficiency because the ranges of the reaction products (α particles and ^7Li ions from $^{10}B(n,\alpha)^7Li$ reaction) are also on the order of 3–4 μm; thicker layers prevent charged products generated deep inside the film from reaching the semiconductor[15,16,44]. Therefore, we quantified the converter areal density by cold-neutron transmission measurementsat 1.3 meV (Fig. 1f), yielding an equivalent ^{10}B thickness of approximately 3.3 μm. Owing to inter-particle voids inherent to electrosprayed films, the physical thickness was ~12 μm, corresponding to a volume density of 0.655 g cm^{-3} (vs. 2.34 g cm^{-3} for theoretical ^{10}B); however, the effective thickness relevant to charge-particle escape remained within the optimal range.

Therefore, we first quantified the effective converter areal density by cold-neutron transmission measurements at 1.3 meV (Fig. 1f), which yielded an equivalent ^{10}B thickness of approximately 3.3 μm[45]. Although electrosprayed films inherently exhibit a reduced packing density, we compensated for this limitation by deliberately increasing the physical thickness of the converter layer. As a result, a ~12 μm-thick electrosprayed film with a volume density of 0.655 g cm^{-3} (compared with 2.34 g cm^{-3} for bulk ^{10}B) provided an effective ^{10}B thickness of

approximately 3.3 μm. Guided by this design strategy and considering the escape range of the reaction products, we therefore conclude that the converter layer was successfully tuned to the target value, enabling near-ideal detection sensitivity.

The converter film was laminated directly onto the Au electrode and encapsulated with a barrier film during assembly (Figs. 1g and 1h). Monte–Carlo simulations (PHITS: Particle and Heavy-Ion Transport code System) [46] revealed that an air gap between the Au electrode and the converter layer reduces the energy deposited in the HOIP device by the charged reaction products owing to their finite range in air (Fig. 1i), thereby decreasing the neutron-induced current. Experimentally, devices assembled with a controlled air gap and those laminated under mechanical tension to eliminate the gap exhibited systematic and reproducible differences in sensitivity under cold-neutron irradiation at 2.4×10^4 s^{-1} cm^{-2} (1.3 meV) (Fig. 1j), in quantitative agreement with the simulation results in Fig. 1i. These results demonstrate that gap-free lamination is a key engineering requirement to maximize energy transfer from the reaction products to the semiconductor and thus to preserve neutron sensitivity. In addition, the rapid onset of the induced current immediately after irradiation and the stable signals acquired at 1-s intervals indicate a negligible transient response (Fig. 1j), supporting the suitability of the device for hour-scale BNCT monitoring.

γ-ray sensitivity was evaluated using a ^{60}Co source (Fig. 1k), comparing devices configured with the converter (WC) and without the converter (WoC). WC devices consistently exhibited lower γ sensitivity than WoC devices, suggesting that the conversion-layer assembly may introduce additional degradation pathways─potentially via moisture release from the ^{10}B film or polyimide within the encapsulation—an effect that is under further investigation. Overall, tailoring the active area to 5×5 mm^2 and equivalent ^{10}B thickness of 3.3 μm enabled BNCT-compatible

spatial resolution and maximized neutron sensitivity while maintaining fast, stable real-time response.

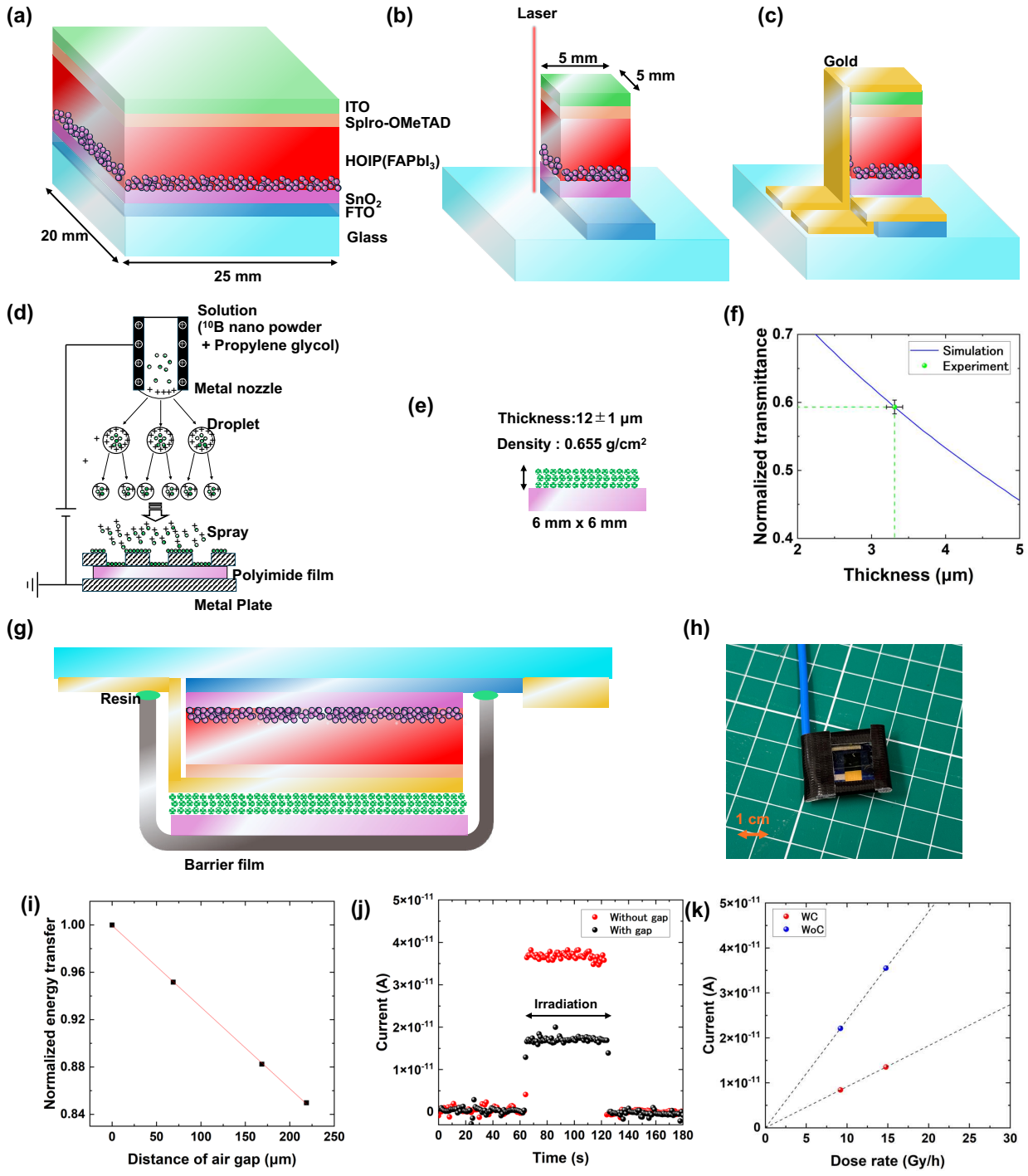


Fig. 1 | Structure and detection characteristics of HOIP neutron sensor: (**a)** layered architecture of the HOIP device (FTO glass/SnO_2/$Cs_{0.05}FA_{0.95}PbI_3$/HTL/ITO) operated in a self-biased photovoltaic configuration, (**b)** laser patterning to define a 5 × 5 mm^2 active area, (**c)** top electrode geometry formed by Au evaporation, (**d)** schematic of ^{10}B conversion film fabrication, (**e)** schematic of the fabricated ^{10}B conversion film, (**f)** converter thickness determined from cold-neutron (1.3 meV) transmission measurements, (**g)** assembly structure of the HOIP device with the ^{10}B conversion film and barrier encapsulation, (**h)** photograph of the assembled HOIP neutron sensor, (**i)** simulated energy deposition in the HOIP device as a function of the air gap between the Au electrode and ^{10}B conversion layer, (**j)** cold-neutron response of the HOIP sensor with and without eliminating the air gap during encapsulation, and (**k)** γ-ray response under ^{60}Co irradiation for WC and WoC devices.

High-flux neutron irradiation in a BNCT facility

We evaluated HOIP sensors in a clinically relevant BNCT environment, i.e., the Heavy Water Neutron Irradiation Facility (HWNIF) at the Kyoto University Research Reactor (KUR)[25], where BNCT has been implemented in clinical practice[47]. The irradiation port (Fig. 2a) and sample-transport rail enabled reproducible positioning of the HOIP sensors fixed on a holder (Fig. 2b) at the standard irradiation position (Fig. 2c), whose neutron and γ-ray fields are well characterized in prior reports[25]. Neutron flux and γ-ray dose were tuned by opening/closing the HWNIF spectrum shifters (SS1–SS3; Table 1).

Figs. 2d and 2e show the time-resolved, radiation-induced currents, recorded at 1-s intervals, for WoC and WC devices, respectively. Increasing the openings of the spectrum shifter (SS) resulted in higher neutron and γ-ray fields, and both device types exhibited clear increases in signal

that scaled with the irradiated neutron flux. WC devices produced currents in the tens-of-nA range whereas WoC devices generated only pA-level currents—nearly four orders of magnitude lower—demonstrating that the measured response in WC devices is dominated by neutron-conversion events rather than γ-ray background. Notably, the background currents measured before and after irradiation remained unchanged, indicating negligible activation-induced self-emission from the readout cables, electrodes, or encapsulation materials and supporting robust in situ monitoring.

Figures 2f and 2g show the induced currents as a function of γ-ray dose (WoC) and neutron flux (WC). The red line in Fig. 2f represents the γ-induced current predicted from ^{60}Co calibration (Fig. 1k). Although the HWNIF γ response was comparable in magnitude, a ~1.3× deviation emerged with increasing SS opening, presumably due to spectral differences between ^{60}Co and facility γ fields, besides reported 20%–30% uncertainties in reference γ-dose values following recent core-configuration changes. While the γ-induced signals were four orders of magnitude smaller than the neutron-induced signals under BNCT-relevant conditions, facility-specific γ-field characterization using WoC devices remains essential. This requirement arises from BNCT operational guidelines that impose upper limits on accompanying γ doses and from the need to accurately subtract γ contributions when performing quantitative neutron dosimetry. Accordingly, WoC-based in-facility γ calibration constitutes a necessary quality-assurance procedure at each BNCT site.

WC currents scale linearly with neutron flux up to the ~10^9-s^{-1} cm^{-2} regime (Fig. 2g), indicating that HOIP sensors are effective for BNCT-relevant high-flux measurements. Because WC signals include both neutron- and γ-induced components, we estimated the γ contribution using the WoC response together with the ~2.6× lower γ sensitivity of WC (Fig. 1k). This analysis yields an extremely small γ-noise fraction of ~0.012% in HWNIF, far below clinical error tolerances.

Collectively, these data demonstrate that HOIP sensors enable accurate, second-scale, real-time neutron-flux monitoring in BNCT fields with essentially negligible γ-ray interference.

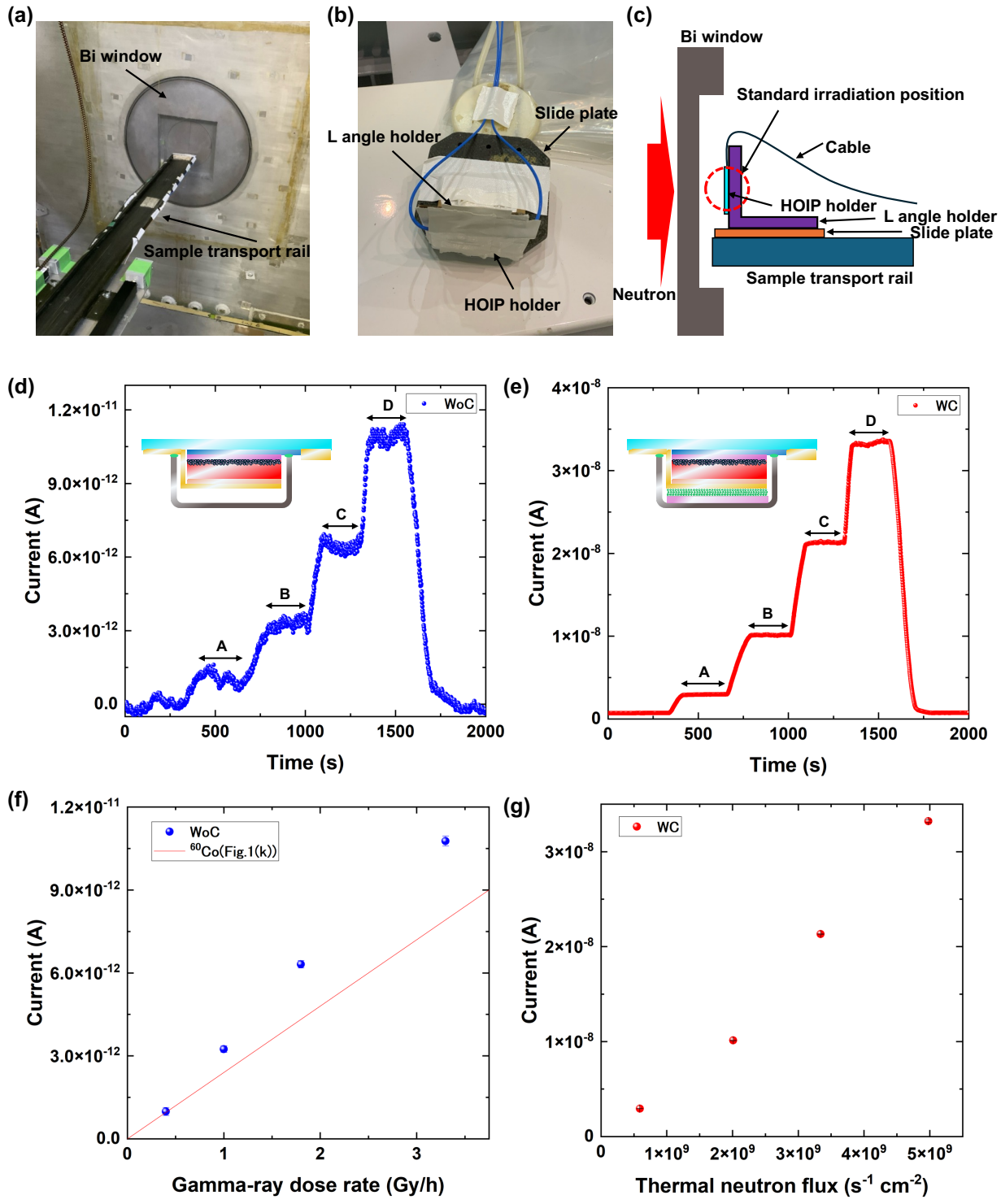


Fig. 2 | Response of HOIP sensors in a BNCT-relevant high-flux neutron field: (**a**) photograph of the HWNIF at KUR, (**b**) photograph of the sample holder used for irradiation tests, (**c**) schematic illustration of the standard irradiation position in HWNIF where the HOIP sensors were placed, (**d**) time-resolved radiation-induced current of the HOIP device without the 10B conversion layer (WoC) during HWNIF irradiation, (**e**) time-resolved radiation-induced current of the HOIP device with the 10B conversion layer (WC) under identical irradiation conditions, (**f**) radiation-induced current of the WoC sensor plotted as a function of γ-ray dose rate in HWNIF, and (**g**) radiation-induced current of the WC sensor plotted as a function of neutron flux in HWNIF.

Table 1 | Neutron flux and γ-ray dose at the standard irradiation position of the KUR-HWNIF as a function of spectrum-shifter settings.

Condition	SS1	SS2	SS3	Thermal neutron flux (s^{-1} cm^{-2})	Gamma ray dose rate (Gy/h)
A	Close	Close	Close	5.90×10^{8}	0.4
B	Open	Close	Close	2.01×10^{9}	1
C	Open	Open	Close	3.34×10^{9}	1.8
D	Open	Open	Open	4.98×10^{9}	3.3

Long-term stability under BNCT-level fluence

BNCT monitoring requires detectors that can withstand neutron fluences up to ~10^{13} cm^{-2} without performance loss. To assess operational stability, we performed prolonged high-flux irradiation of HOIP sensors at HWNIF (D condition). (Fig. 3a). Fig. 3b shows the normalized induced current during irradiation plotted against accumulated neutron fluence. No detectable

degradation was observed up to 10^{13} cm^{-2}, indicating excellent radiation tolerance under BNCT-relevant exposure.

In HOIP sensors, degradation is expected to be driven more strongly by energetic charged products (α particles and ^{7}Li ions) generated in the ^{10}B layer than by non-ionizing neutron energy loss in the semiconductor[42]. Nevertheless, WoC devices—serving as a reference without charged-particle injection—exhibited fluctuation trends similar to WC devices, suggesting that time-dependent signal variations mainly reflect reactor-power instability rather than intrinsic device deterioration.

We compared I–V characteristics before and after neutron exposure to capture subtle irradiation effects (Fig. 3c). A modest increase in current was observed at biases above ~1 V, consistent with an increased density of recombination centers. Such defect formation can contribute to radiation-induced current; however, it does not necessarily translate into immediate sensitivity loss[48]. The induced signal degrades only when the carrier diffusion length becomes shorter than the HOIP layer thickness[49,50]. Given the ultra-thin (~500 nm) HOIP absorber used in this study, the device is relatively insensitive to moderate recombination-center increases, explaining the stable neutron-induced currents[51]. Although longer exposures may eventually cause degradation, these results demonstrate that HOIP sensors retain high stability up to the clinically required BNCT fluence.

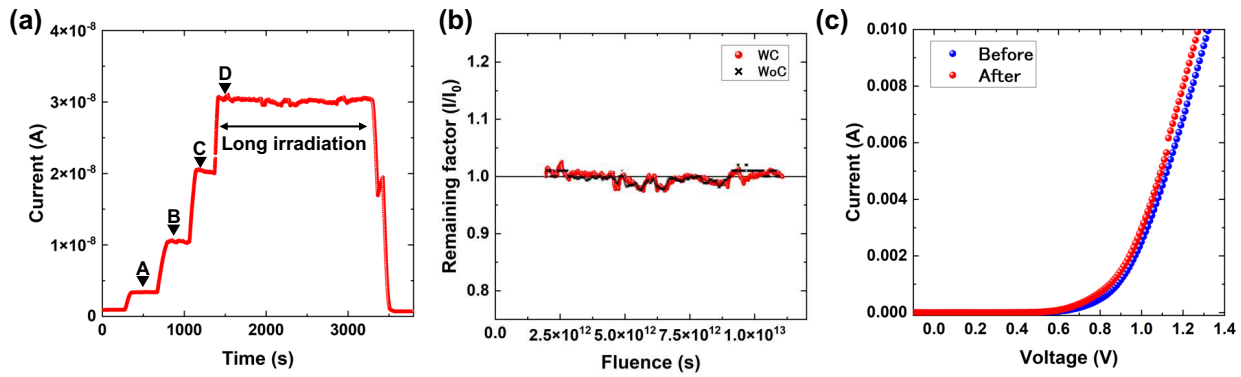


Fig. 3 | Degradation behavior of HOIP sensors under BNCT-relevant irradiation: **(a)** time evolution of the radiation-induced current of the WC HOIP sensor during prolonged high-flux neutron irradiation in HWNIF, **(b)** retained (normalized) current signals of WC and WoC devices as a function of accumulated neutron fluence during long-duration irradiation, and **(c)** I–V characteristics measured before and after irradiation, revealing subtle changes in device properties.

Benchmarking against BNCT real-time monitoring requirements

BNCT clinical guidelines emphasize real-time neutron monitoring, motivating direct comparison with established dosimetry approaches. Table 2 summarizes the performance of the fabricated HOIP sensors relative to ^{197}Au activation[26] and Eu-doped LiCAF scintillator[27] methods. The HOIP sensors meet the required spatial resolution by design ($<5 \times 5$ mm^2), and their active area can be further reduced by laser patterning for higher localization, if needed. Although smaller areas decrease signal magnitude, the present noise floor indicates that signals an order of magnitude lower than neutron induced current levels remain detectable, suggesting that miniaturization to ~2.5 mm² is feasible in future implementations.

The aggregate measurement error of HOIP sensors—accounting for γ-ray noise, radiation effects, and signal fluctuation—remains less than 5%, comparable to conventional monitors and within clinical tolerances. Linearity over broad neutron-flux ranges has been indicated previously (10^5–10^{12} s^{-1} cm^{-2})[42], and we confirm the linear response in the BNCT-relevant ~10^9-s^{-1} cm^{-2} regime. Moreover, as HOIP devices employ a photovoltaic architecture, pre-irradiation optical inspection and I–V measurements provide a practical route for integrity screening, offering an additional quality-control advantage over existing techniques.

With 1-s signal acquisition, simple electrical cabling, and standard current readout, real-time operation is achieved. Although copper cables can exhibit minor activation immediately after irradiation, the resulting impact is expected to be manageable; nonetheless, engineering low-activation conductors (e.g., carbon-based cables) will further strengthen clinical translation. Overall, these results verify that HOIP sensors provide guideline-compliant, high-accuracy real-time neutron-flux monitoring in BNCT fields, establishing their utility as practical dosimetry and safety-assurance tools during therapy.

258

259 **Table 2 |** Performance comparison of BNCT monitoring requirements with conventional neutron
260 dosimetry methods (^{197}Au activation and LiCAF scintillators) and the present HOIP sensor,
261 based on clinical BNCT guidelines.

Specification	Reqirement	HOIP Current study	LiCAF	Au Foil Activation Method	HOIP further study
Position resolution	x:≦5 mm y:≦5 mm	x:5 mm y: 5 mm	x:<1 mm y:<1 mm	x:1–5 mm y:1–5 mm	x:1–5 mm y:1–5 mm
Calibration test	Necessary	High-flux neutron field	High-flux neutron field	Wight of Au foil	Light calibration method
γ-ray noise (Few Gy/h)	<5%	0.01%	close to zero	0%	
Radiation degradation (10^{13} cm^{-2})	<5%	close to zero	close to zero	close to zero	
Neutron sensitivity (s^{-1} cm^{-2})	~10^{9}	10^{5}~10^{12}	10^{5} ~ 10^{10}	All	
Time resolution	Few second	1 s	1 s	-	
Signal Fluctuation	<5%	<1%	3.3%	-	

(1 h)					
Response to B drugs	No correction	No correction	1/v behavior correction	1/v behavior correction	
Install on human body	-	Medical tape	Medical tape	Medical tape	Wearable sensor technology
Measurement error	<5%	<1%	3.3%	-	
Signal transport method	-	Coaxial cable	Carbon cable	-	Carbon cable
Signal Measurement	-	Ammeter	PMT, MCA	HPGe	
Pre-use check	Necessary	I–V characteristics	Difficult	Eu γ-ray for HPGe	

Methods

Preparation of HOIP thin-film devices

The device structure we employed was FTO glass/SnO_2/$Cs_{0.05}FA_{0.95}PbI_3$/HTL/ITO. FTO glass substrates were ultrasonically cleaned sequentially with ultrapure water and ethanol followed by UV-ozone cleaning. The compact SnO_2 layer was deposited from a mixed aqueous solution of SnO_2 and an alkali halide dopant through a spin-coating process followed by annealing for 30min. The FTO/SnO_2 layer was exposed to the UV-ozone cleaner and quickly transferred to the glove box, where mixed solution of PbI_2 and CsI was deposited by spin coating method. Then, FAI and

additives dissolved in IPA were spin-coated onto the PbI_2+CsI layer followed by annealed. For the HTL layer, Spiro-OMeTAD was dissolved in chlorobenzene with some dopants and dynamically spin-coated on the passivation layer. Then ITO was deposited by DC sputtering. The area of each cell is designated as 25.0 mm^2 (5.0 x 5.0 mm) by means of a laser pattering. Finally, gold was thermally evaporated using a mask as a grid on ITO. The spin-coating processes described above are performed in a dry air condition up to the annealing of perovskite layer and switch to N_2 from the following process.

Preparation of ^{10}B conversion films

HOIP devices were supplied by PXP Co., Ltd. ^{10}B-enriched boron powder (>96% ^{10}B, d90 < 23 μm; 3M) was milled into nanoparticles using a planetary bead mill (Thinky, NP-100). For each milling cycle, 4-g boron powder, 12-g deionized water, and 35-g 500-μm-diameter Al_2O_3 beads were loaded into an Al_2O_3 container. Milling was performed at 1500 rpm for 1 min per cycle, repeated for 30 cycles with 2-min cooling intervals between cycles. The resulting nanoparticles exhibited a size distribution shown in Fig. 4 (d90 < 257 nm).

For electrospray deposition[52,53], 26 mL of the boron nanoparticle dispersion was mixed with 16 mL of propylene glycol to obtain a boron concentration of 2 wt%. The solution was electrosprayed through a 0.1-mm-diameter metal needle under an applied voltage of 10 kV at a flow rate of 0.02 mL min^{-1}. The spray was deposited onto polyimide films (thickness: 0.1 mm) maintained at 90°C. The substrate was translated on an XY stage at 10 mm s^{-1} to achieve uniform coating over the full substrate area, and the scan was repeated 30 times.

The areal density of the fabricated ^{10}B conversion films was evaluated by cold-neutron transmission measurements (>1.3 meV) at the MINE beamline of JRR-3. The transmission was

determined by comparing the ^{3}He detector count rates for three configurations listed in Table 3: (i) a bare beam (no sample), (ii) a polyimide film only, and (iii) a polyimide film coated with the ^{10}B layer. Here, “Counts (vol.1)” and “Counts (vol.2)” indicate two independent measurement runs performed under identical beam and detector conditions to confirm reproducibility. From these measurements, the neutron transmission of the ^{10}B-coated film was estimated to be 59.3%. hich was converted into an equivalent ^{10}B thickness using the Monte–Carlo simulation results shown in Fig. 1f. Because the cold-neutron beam at 1.3 meV has a finite energy spread, the equivalent ^{10}B thickness of 3.3 μm derived from the transmission measurements represents a spectrum-averaged effective value, and the true physical-equivalent thickness may slightly deviate from this value.

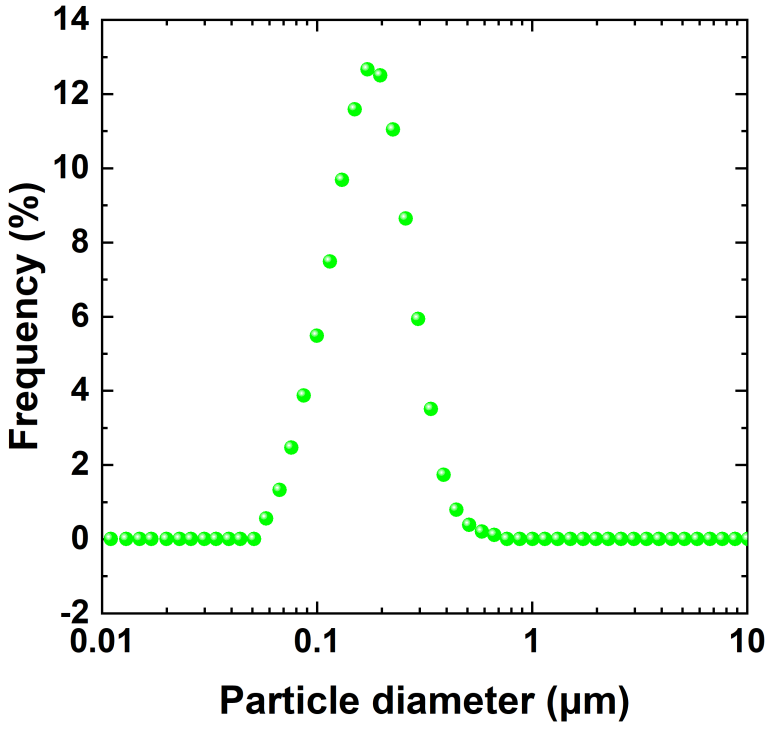


Fig. 4 | Particle-size distribution of ^{10}B boron nanoparticles; size distribution of the milled ^{10}B powder after bead milling, showing d90 <257 nm.

Table 3 | Cold-neutron transmission of the ^{10}B conversion film.

"Counts (vol.1)" and "Counts (vol.2)" denote two independent measurements conducted under identical experimental conditions.

Condition	Counts (vol.1)	Counts (vol.2)
(i) Bare	1800011	1790248
(ii) Polyimide film	1671701	1722638
(iii) Sample 1	1012526	1008229
(iv) Sample 2	1006455	1001806
(iii) Sample 3	1008466	1004230

Radiation-induced current measurements

Radiation-induced currents from the HOIP sensors were recorded using a source-measure unit (SMU; Keysight B2912A) connected via a coaxial cable. All irradiation measurements were performed in a self-biased mode with 0-V applied voltage. The current was acquired with a sampling integration interval of 1 s. I–V characteristics were measured using the same SMU before and after irradiation for degradation assessment.

References

1. Tanabe, K. et al.. Compact and transportable system for detecting lead - shielded highly enriched uranium using ^{252}Cf rotation method with a water Cherenkov neutron detector. *Sci. Rep.* **14**, 18828 (2024).

2. Favalli, A. et al.. Next-generation neutron detection using a Li glass scintillator composite *Commun. Phys.* **8**, 10 (2025).

3. van der Ende B. M., Li, L., Godin, D., and Sur B., Stand-off nuclear reactor monitoring with neutron detectors for safeguards and non-proliferation applications. *Nat. Commun*. **10**, 1959 (2019).

4. Tanabe, K. et al. Development of a water Cherenkov neutron detector for the active rotation method and demonstration of nuclear material detection. *J. Nucl. Sci. Technol.* **60**, 769-781 (2023).

5. Favalli, A. et al. Demonstration of active neutron interrogation of special nuclear materials using a high-intensity short-pulse-laser-driven neutron source. *Sci Rep* **15**,724 (2025).

6. Ikeda, Y., Otake, Y. & Mizuta, M. Nondestructive measurement method to detect water/void inside slabs using compact neutron source by backscattered neutrons. *J. Adv. Concr. Technol.* **15**, 603-609 (2017).

7. Ikeda, Y. et al. Prospect for application of compact accelerator-based neutron source to neutron engineering diffraction. *Nucl. Instruments Methods Phys. Res. Sect. A Accel. Spectrometers, Detect. Assoc. Equip.* **833**, 61-67 (2016).

8. Wakabayashi, Y. et al. A study on the non-destructive detection of salt in concrete using neutron-captured prompt-gamma rays at RANS. *Plasma Fusion Res.* **13**, 2-5 (2018).

9. Ikeda, S., Otake, Y., Kobayashi, T. & Hayashizaki, N. Design of 500 MHz RFQ linear accelerator for a compact neutron source, RANS-III. *Nucl. Instruments Methods Phys. Res. Sect. B Beam Interact. with Mater. Atoms* **461**, 186-190 (2019).

10. Zhang, Z. & Liu, T. A review of the development of in-hospital neutron irradiator-1 and boron neutron capture therapy clinical research on malignant melanoma. *Ther. Radiol. Oncol.* **2**, 49-49 (2018).

11. Goodhead, D. T. Neutrons are forever! Historical perspectives. *Int. J. Radiat. Biol.* **95**, 957-984 (2019).

12. Ishikawa, M. et al. Development of real-time thermal neutron monitor using boron-loaded plastic scintillator with optical fiber for boron neutron capture therapy. *Appl. Radiat. Isot.* **61**, 775-779 (2004).

13. Ishikawa, M. et al. Early clinical experience utilizing scintillator with optical fiber (SOF) detector in clinical boron neutron capture therapy: its issues and solutions. *Radiat. Oncol.* **11**, 1-10 (2016).

14. Chica, D. G. et al. Direct thermal neutron detection by the 2D semiconductor 6LiInP2Se6. *Nature* **577**, 346-349 (2020).

15. Bhattarai, G., Caruso, A. N. & Paquette, M. M. Single-carrier charge collection in thin direct-conversion semiconductor neutron detector: a numerical simulation. *J. Appl. Phys.* **129**, 194502 (2021).

16. McGregor, D. S., Hammig, M. D., Yang, Y. H., Gersch, H. K. & Klann, R. T. Design considerations for thin film coated semiconductor thermal neutron detectors - I: basics regarding alpha particle emitting neutron reactive films. *Nucl. Instruments Methods Phys. Res. Sect. A Accel. Spectrometers, Detect. Assoc. Equip.* **500**, 272-308 (2003).

17. Pietropaolo, A. et al. Neutron detection techniques from μeV to GeV. *Phys. Rep.* **875**, 1-65 (2020).

18. Höglund, C. et al. B 4C thin films for neutron detection. *J. Appl. Phys.* **111**, 104908 (2012).

19. Kobayashi, T., Sakurai, Y. & Ishikawa, M. A noninvasive dose estimation system for clinical BNCT based on PG-SPECT - Conceptual study and fundamental experiments using HPGe and CdTE semiconductor detectors. *Med. Phys.* **27**, 2124-2132 (2000).

20. Caruso, A. N. The physics of solid-state neutron detector. *J. Phys. Condens. Matter* **22**, 13-21 (2010).

21. Matsubayashi, N. et al. Air ionization chamber combined with LiCaAlF6 scintillator for γ-ray dose evaluation in boron neutron capture therapy. *Nucl. Instruments Methods Phys. Res. Sect. A Accel. Spectrometers, Detect. Assoc. Equip.* **1047**, 167883 (2023).

Therapy (BNCT) Irradiation System: Development Guidelines. Economic and industrial policy bureau, ministry of economy, trade and industry (METI) & Japan agency for medical research and development (AMED). https://www.meti.go.jp/policy/mono_info_service/healthcare/iryou/downloadfiles/pdf/45_guideline.pdf (2019).

23. Colonna, N., Gunsing, F. & Käppeler, F. Neutron physics with accelerators. *Prog. Part. Nucl. Phys.* **101**, 177-203 (2018).

24. Nakamura, S. et al. Modeling the detection efficiency of an HP-Ge detector for use in boron neutron capture therapy. *Appl. Radiat. Isot.* **125**, 80-85 (2017).

25. Sakurai, Y. & Kobayashi, T. Spectrum evaluation at the filter-modified neutron irradiation field for neutron capture therapy in Kyoto University Research Reactor. *Nucl. Instruments Methods Phys. Res. Sect. A Accel. Spectrometers, Detect. Assoc. Equip.* **531**, 585-595 (2004).

26. Suzuki, S. et al. Initial evaluation of accelerator-based neutron source system at the Shonan Kamakura General Hospital. *Appl. Radiat. Isot.* **199**, 110898 (2023).

27. Jeon, S. J., Choi, J., Lee, K. Y. & Yi, J. Real-time neutron beam monitor utilizing scintillator technology for boron neutron capture therapy. *Radiat. Meas.* **172**, 107070 (2024).

28. Watanabe, K. et al. Development of an optical fiber type detector using a Eu:LiCaAlF6 scintillator for neutron monitoring in boron neutron capture therapy. *Nucl. Instruments Methods Phys. Res. Sect. A Accel. Spectrometers, Detect. Assoc. Equip.* **802**, 1-4 (2015).

29. Miyazawa, Y. et al. Tolerance of perovskite solar cell to high-energy particle irradiations in space environment. *iScience* **2**, 148-155 (2018).

30. Yu, D. et al. Two-dimensional halide perovskite as β-ray scintillator for nuclear radiation monitoring. *Nat. Commun.* **11**, 1-10 (2020).

31. Pérez-del-Rey, D. et al. Perovskite solar cells: stable under space conditions. *Sol. RRL* **4**, 1-6 (2020).

32. Kirmani, A. R. et al. Unraveling radiation damage and healing mechanisms in halide perovskites using energy-tuned dual irradiation dosing. *Nat. Commun.* **15**, 696 (2024).

33. Fru, J. N. & Diale, M. Abnormal high stability halide perovskite thin films and solar cells to alpha and gamma irradiations with varying fluence. *Radiat. Phys. Chem.* **216**, 111480 (2024).

34. Mescher, H. et al. Flexible inkjet-printed triple cation perovskite X-ray detectors. *ACS Appl. Mater. Interfaces* **12**, 15774-15784 (2020).

35. Guo, J. et al. High-stability flexible X-ray detectors based on lead-free halide perovskite Cs2TeI6 films. *ACS Appl. Mater. Interfaces* **13**, 23928-23935 (2021).

36. Huang, K. et al. γ-ray radiation on flexible perovskite solar cells. *ACS Appl. Energy Mater.* **3**, 7318-7324 (2020).

37. Jena, A. K., Kulkarni, A. & Miyasaka, T. Halide perovskite photovoltaics: background, status, and future prospects. *Chem. Rev.* **119**, 3036-3103 (2019).

38. Hu, A. et al. Ultraelastic lead halide perovskite films via direct laser patterning. *ACS Nano* **19**, 2286-2293 (2025).

39. Mao, W. et al. Laser patterning of large-scale perovskite single-crystal-based arrays for single-mode laser displays. *Int. J. Extrem. Manuf.* **5**, 045001 (2023).

40. Uppara, B. et al. Optimization of laser patterning process for eco-friendly tin-halide perovskite solar module – with a nanosecond green laser. *Thin Solid Films* **807**, 140542 (2024).

41. Hu, J. et al. Full-color and high-resolution femtosecond laser patterning of perovskite quantum dots in polyacrylonitrile matrix. *Adv. Funct. Mater.* **34**, 1-8 (2024).

42. Okuno, Y. et al. Hybrid organic – Inorganic perovskite semiconductor-based high- flux neutron detector with BN converter. *ACS Appl. Electron. Mater.* **4**, 3411-3420 (2022).

43. Okuno, Y. et al. Potential for radiation detector based on Si , InGaP , CIGS , and perovskite solar cells. *Jpn. J. Appl. Phys.* **64**, 06SP09 (2025).

44. Caricato, A. P. et al. Thermal neutron conversion by high purity 10B-enriched layers: PLD-growth, thickness-dependence and neutron-detection performances. *Eur. Phys. J. Plus* **137**, 431 (2022).

45. Safavi, S. M. et al. Preparation and characterization of a new Gd2O3-epoxy composite for neutron shielding applications. *Sci. Rep.* **14**, 1-15 (2024).

46. Iwamoto, Y. et al. Benchmark study of particle and heavy-ion transport code system using shielding integral benchmark archive and database for accelerator-shielding experiments. *J. Nucl. Sci. Technol.* **59**, 665-675 (2022).

47. IAEA. *Current status of neutron capture therapy*. IAEA-TECDOC-1223 (2001).

48. Y. Okuno, S. Okuda, M. Akiyoshi, T. Oka, M. Harumoto, K. Omura, S. Kawakita, M. Imaizumi, S. R. Messenger, K. H. Lee, M. Y.48. Okuno, Y. et al. Radiation degradation

prediction for InGaP solar cells by using appropriate estimation method for displacement threshold energy. *J. Appl. Phys.* **122**, 114901 (2017).

49. Okuno, Y., Okuda, S., Oka, T., Kawakita, S. & Imaizumi, M. Performance degradation of InGaP solar cells due to 70 keV electron irradiation. *Jpn. J. Appl. Phys.* **56**, 081203 (2017).

50. Yamaguchi, M. Radiation-resistant solar cells for space use. *Sol. Energy Mater. Sol. Cells* **68**, 31-53 (2001).

51. Messenger, G. C. & Spratt, J. P. The effects of neutron irradiation on germanium and silicon. *Proc. IRE* **99**, 1038-1044 (1956).

52. Park, S. H. *et al.* Efficient electrospray deposition of surfaces smaller than the spray plume. *Nat. Commun.* **14**, 1–9 (2023).

53. Li, S. *et al.* Electrospray deposition device used to precisely control the matrix crystal to improve the performance of MALDI MSI. *Sci. Rep.* **6**, 1–10 (2016).

Acknowledgements

This work was supported by JAEA Nuclear Energy S&T and Human Resource Development Project through concentrating wisdom Grant No. JPMXDO220354241 and JPJA22P226 83601. This work was supported in part by the Ministry of Education, Culture, Sports, Science and Technology of Japan(MEXT) under the Nuclear Energy Systems Research and Development Project JPMXD0212345678. A part of this study was carried out in the Joint Research Project "Research and Development for the Decommissioning of Fukushima Daiichi Nuclear Power Plants" by Tohoku University and Fukushima Daiichi D&D Engineering Company, TEPCO Holdings, Inc.

461

462 **Ethics Declarations**

463 The authors declare no competing interests.